Non-invasive carotid imaging using optoacoustic tomography

Alexander Dima and Vasilis Ntziachristos*

Institute for Biological and Medical Imaging, Technische Universität München und Helmholtz Zentrum München, Ingoldstädter Landstrasse 1, 85764 Neuherberg, Germany
**v.ntziachristos@tum.de*

Abstract: The high prevalence of atherosclerosis and the corresponding derived morbidity drives the investigation of novel imaging tools for disease diagnosis and assessment. Multi-spectral optoacoustic tomography (MSOT) can resolve structural, hemodynamic and molecular parameters that relate to cardiovascular disease. Similarly to ultrasound imaging, optoacoustic (photoacoustic) imaging can be implemented as a handheld arrangement which further brings dissemination potential to point of care applications. Correspondingly, we experimentally investigate herein the performance of non-invasive optoacoustic scanning developed for carotid imaging, in phantoms and humans. The results demonstrate that traditional transducers employed in ultrasound imaging do not offer optimal MSOT imaging. Instead, feasibility to detect human carotids and carotid-sized vessels in clinically-relevant depths is better demonstrated with curved arrays and tomographic approaches.

OCIS codes: (170.0170) Medical optics and biotechnology; (170.0110) Imaging systems; (170.5120) Photoacoustic imaging; (170.1610) Clinical applications.

References and links

1. A. S. Jahromi, C. S. Cinà, Y. Liu, and C. M. Clase, "Sensitivity and specificity of color duplex ultrasound measurement in the estimation of internal carotid artery stenosis: a systematic review and meta-analysis," J. Vasc. Surg. **41**(6), 962–972 (2005).
2. A. Long, A. Lepoutre, E. Corbillon, and A. Branchereau, "Critical Review of Non- or Minimally Invasive Methods (Duplex Ultrasonography, MR- and CT-angiography) for Evaluating Stenosis of the Proximal Internal Carotid Artery," Eur. J. Vasc. Endovasc. Surg. **24**(1), 43–52 (2002).
3. D. Huang, E. A. Swanson, C. P. Lin, J. S. Schuman, W. G. Stinson, W. Chang, M. R. Hee, T. Flotte, K. Gregory, C. A. Puliafito, and et, "Optical coherence tomography," Science **254**(5035), 1178–1181 (1991).
4. A. Rosencwaig and P. R. Griffiths, "Photoacoustics and Photoacoustic Spectroscopy," Phys. Today **34**(6), 64–66 (1981).
5. R. A. Kruger, P. Liu, Y. R. Fang, and C. R. Appledorn, "Photoacoustic ultrasound (PAUS)--Reconstruction tomography," Med. Phys. **22**(10), 1605–1609 (1995).
6. X. Wang, Y. Pang, G. Ku, X. Xie, G. Stoica, and L. V. Wang, "Noninvasive laser-induced photoacoustic tomography for structural and functional in vivo imaging of the brain," Nat. Biotechnol. **21**(7), 803–806 (2003).
7. M. J. Colles, N. R. Geddes, and E. Mehdizadeh, "The optoacoustic effect," Contemp. Phys. **20**(1), 11–36 (1979).
8. Y. Wang, X. Xie, X. Wang, G. Ku, K. L. Gill, D. P. O'Neal, G. Stoica, and L. V. Wang, "Photoacoustic Tomography of a Nanoshell Contrast Agent in the in Vivo Rat Brain," Nano Lett. **4**(9), 1689–1692 (2004).
9. D. Razansky, C. Vinegoni, and V. Ntziachristos, "Multispectral photoacoustic imaging of fluorochromes in small animals," Opt. Lett. **32**(19), 2891–2893 (2007).
10. H.-P. Brecht, R. Su, M. Fronheiser, S. A. Ermilov, A. Conjusteau, and A. A. Oraevsky, "Whole-body three-dimensional optoacoustic tomography system for small animals," J. Biomed. Opt. **14**(6), 064007–064008 (2009).
11. A. Buehler, E. Herzog, D. Razansky, and V. Ntziachristos, "Video rate optoacoustic tomography of mouse kidney perfusion," Opt. Lett. **35**(14), 2475–2477 (2010).
12. A. A. Oraevsky, A. A. Karabutov, S. V. Solomatin, E. V. Savateeva, V. A. Andreev, Z. Gatalica, H. Singh, and R. D. Fleming, "Laser optoacoustic imaging of breast cancer in vivo," in *Biomedical Optoacoustics II*, (SPIE, 2001), 6–15.
13. J. J. Niederhauser, M. Jaeger, R. Lemor, P. Weber, and M. Frenz, "Combined ultrasound and optoacoustic system for real-time high-contrast vascular imaging in vivo," IEEE Trans. Med. Imaging **24**(4), 436–440 (2005).

#166684 - $15.00 USD Received 13 Apr 2012; revised 30 Jul 2012; accepted 30 Jul 2012; published 18 Oct 2012

14. C. Haisch, K. Eilert-Zell, M. M. Vogel, P. Menzenbach, and R. Niessner, "Combined optoacoustic/ultrasound system for tomographic absorption measurements: possibilities and limitations," Anal. Bioanal. Chem. **397**(4), 1503–1510 (2010).
15. C. Kim, T. N. Erpelding, L. Jankovic, M. D. Pashley, and L. V. Wang, "Deeply penetrating in vivo photoacoustic imaging using a clinical ultrasound array system," Biomed. Opt. Express **1**(1), 278–284 (2010).
16. V. Ntziachristos and D. Razansky, "Molecular Imaging by Means of Multispectral Optoacoustic Tomography (MSOT)," Chem. Rev. **110**(5), 2783–2794 (2010).
17. D. Razansky, C. Vinegoni, and V. Ntziachristos, "Mesoscopic imaging of fluorescent proteins using multi-spectral optoacoustic tomography (MSOT)," in (SPIE, 2009), 71770D–71776.
18. A. Rosenthal, D. Razansky, and V. Ntziachristos, "Fast semi-analytical model-based acoustic inversion for quantitative optoacoustic tomography," IEEE Trans. Med. Imaging **29**(6), 1275–1285 (2010).
19. A. Buehler, A. Rosenthal, T. Jetzfellner, A. Dima, D. Razansky, and V. Ntziachristos, "Model-based optoacoustic inversions with incomplete projection data," Med. Phys. **38**(3), 1694–1704 (2011).
20. J. Glatz, N. C. Deliolanis, A. Buehler, D. Razansky, and V. Ntziachristos, "Blind source unmixing in multi-spectral optoacoustic tomography," Opt. Express **19**(4), 3175–3184 (2011).
21. M. P. Fronheiser, S. A. Ermilov, H.-P. Brecht, A. Conjusteau, R. Su, K. Mehta, and A. A. Oraevsky, "Real-time optoacoustic monitoring and three-dimensional mapping of a human arm vasculature," J. Biomed. Opt. **15**(2), 021305–021307 (2010).
22. V. Ntziachristos, A. Leroy-Willig, and B. Tavitian, *Textbook of in vivo imaging in vertebrates* (Wiley, 2007).
23. M. J. Niedre, R. H. de Kleine, E. Aikawa, D. G. Kirsch, R. Weissleder, and V. Ntziachristos, "Early photon tomography allows fluorescence detection of lung carcinomas and disease progression in mice in vivo," Proc. Natl. Acad. Sci. U.S.A. **105**(49), 19126–19131 (2008).
24. R. Ma, A. Taruttis, V. Ntziachristos, and D. Razansky, "Multispectral optoacoustic tomography (MSOT) scanner for whole-body small animal imaging," Opt. Express **17**(24), 21414–21426 (2009).

1. Introduction

Carotid artery disease (CAD) is a leading cause of stroke and an indication for other symptoms and diseases, including coronary artery disease. Identification of carotid bruit during a physical examination may lead to recommendations for carotid duplex ultrasonography (DUS) [1], i.e. the combination of conventional anatomical ultrasound and Color Doppler ultrasound. DUS is a portable and cost-effective method that can detect carotid artery stenosis with high sensitivity. Transient ischemic attack, i.e. a non-permanent neurologic dysfunction caused by ischemia, dizziness or a history indicating high-risk for stroke or cardiovascular disease is also an indication for carotid imaging. Carotid artery imaging is also recommended after carotid artery endarterectomy or stenting. Besides ultrasonography, computed tomography angiography (CTA) and magnetic resonance angiography (MRA) may be also administered for carotid artery inspection [2]. Even though CTA and MRA can offer images of the vascular system through the entire volume imaged, DUS is more widely employed for carotid imaging as it offers point-of-care applications without using contrast agents or ionizing radiation.

Optoacoustic imaging is an alternative modality that resolves optical contrast with ultrasonic spatial resolution and can be also considered for carotid imaging. Although tissue-sectioning optical methods such as optical coherence tomography (OCT) and confocal or two-photon microscopy are capable of producing high resolution cross-sectional tissue images, they are limited to imaging depths of a few hundred microns or up to 1-2 mm for OCT [3]. High-resolution optical imaging deeper in biological media is generally prevented by photon scattering in tissues, unless optoacoustic methods are considered [4–6]. Optoacoustic imaging is based on the excitation of ultrasonic waves within tissue, following the absorption of photons with varying intensity [7]. Operationally, it relates to DUS imaging and several scanners have been reported that are based on a clinical ultrasound sensor or they are built with geometrical characteristics that resemble those of an ultrasound sensor. However, despite the use of ultrasonic waves, the method is fundamentally an optical imaging method; the contrast resolved is optical and the depth penetration is also primarily limited by light attenuation in tissues. Therefore, the contrast offered is highly complementary to DUS. In particular, multi-spectral optoacoustic tomography (MSOT) cannot-only resolve anatomical contrast but can also visualize oxygenated and de-oxygenated hemoglobin and a large range of optical agents, probes and nano-particles. This feature can be employed to visualize

#166684 - $15.00 USD Received 13 Apr 2012; revised 30 Jul 2012; accepted 30 Jul 2012; published 18 Oct 2012

molecular tissue changes, not only anatomical biomarkers such as stenosis, and relates closely to the evaluation of treatment protocols and or post-procedural follow-up.

Since optoacoustic imaging depth is defined by photon propagation, and to a certain extent on ultrasonic attenuation depending on the frequency considered, the penetration depth of the technology is limited to relatively superficial tissues compared to other radiologic modalities such as X-ray Computed Tomography or Magnetic Resonance Imaging. So far, optoacoustic imaging, under various implementations such as MSOT or Photo-Acoustic Tomography (PAT) has been predominantly used in small animal imaging mostly on rodents [8–11]. Human diagnostic imaging has been considered as well with initial proof of principle studies focusing on breast cancer [12] and hand vasculature imaging [13]. While the first diagnostic system was stationary and dedicated to breast cancer imaging, later developments have sought to combine optoacoustic and echo-ultrasound into a single handheld device. A few investigations have demonstrated potential for deep tissue capacity [14, 15] and in particular for needle guidance in sentinel lymph node biopsy. However, the appropriateness of optoacoustic carotid imaging and the corresponding performance achieved is not known. We investigated therefore the features and performance of carotid MSOT. The imaging characteristics are demonstrated on controlled carotid-simulating phantoms, considering typical depths of 2-3 cm, in analogy to previous implementations considered in more superficial depths [9, 16, 17]. The previously undocumented ability to detect the human jugular veins and the carotid is also demonstrated.

2. Materials and methods

2.1 Acoustic detection

We have considered two detection geometries with clinical relevance. A conventional clinical linear ultrasound array and a curved ultrasound array were chosen for MSOT detection.

As in previous studies [13, 14] we employed a standard linear ultrasound array probe (Acuson L7, Siemens Healthcare). The probe had 128 elements and was designed to be operated from 5 – 7 MHz in vascular ultrasonography. The element array was weakly focused in the plane of interest (B-scan mode) by an acoustic lens. Individual elements had a pitch of 300 μm and a focal depth of 19 mm. The overall array dimension was 4 mm in height and 38.4 mm in length. For optoacoustic imaging slice thickness in elevation was determined to be 3 mm at the focal point. Figure 1(a) shows the geometrical characteristic of the linear transducer.

The study also employed a curved array of 80 mm diameter, as described in ref [11]. The array consisted of 64 detection elements arranged on a half-arc spanning 172° and 40 mm radius. The array was optimized for a central frequency of 5 MHz and a high input impedance of the DAQ. Individual elements were mechanically focused in elevation (perpendicular to the imaging plane) to achieve a slice thickness of 1 mm measured as full width half maximum (FWHM). Combined the 64 elements provided a region of interest (ROI) in plane of 20 mm x 20 mm around the center of the circle described by the curvature. The ROI is defined as the region in which an elevational resolution of 1 mm and cross-sectional resolution of 150 μm can be achieved. Figure 1(b) shows a schematic of the transducer.

#166684 - $15.00 USD Received 13 Apr 2012; revised 30 Jul 2012; accepted 30 Jul 2012; published 18 Oct 2012

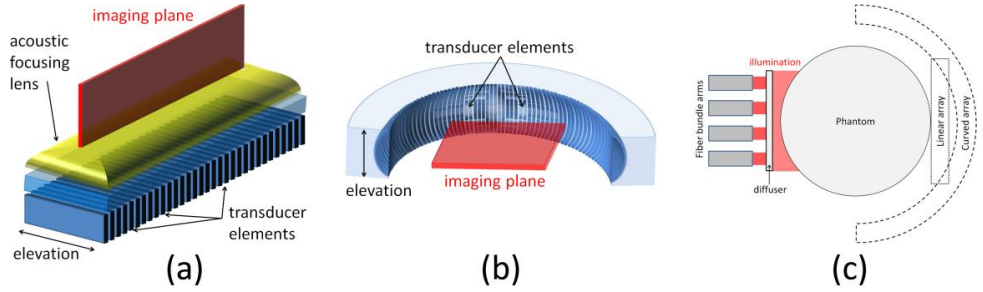

Fig. 1. Detection geometries: (a) L7 linear ultrasound array; (b) curved array. (c) Illumination and detection pattern.

2.2 Phantoms

In order to characterize and compare the optoacoustic imaging performance of detection geometries examined herein, we have chosen two imaging target configurations to simulate clinical application. Both configurations are based on a cylindrical "background" medium (agar based or porcine tissue) of 60 mm diameter and 60 mm height. In the first configuration (type A), depicted in Fig. 2(a), we inserted a transparent cylindrical Tygon tube of 7 mm outer and 5 mm inner diameter concentrically into the background medium. The type A configuration was employed to examine the sensitivity and the overall image quality of the two detection arrays employed. In the second configuration we extended type A by inserting a second clear cylindrical Tygon tube of 3 mm outer and 1 mm inner diameter into the 5 mm diameter tube, as shown in Fig. 2(b). We termed this second configuration as "type B". The type B configuration allows us to examine the ability of resolving an agent in the environment of strong absorbers.

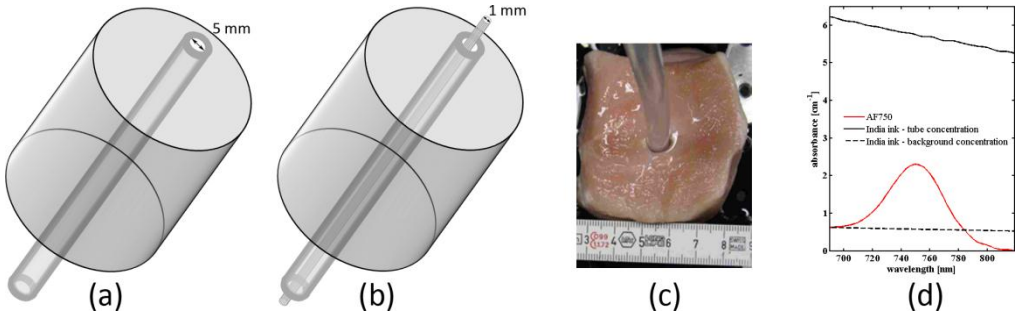

Fig. 2. Phantom properties: (a) Type A configuration. (b) Type B configuration. (c) Porcine muscle phantom. (d) Spectra of employed absorbers.

To evaluate the sensitivity achieved as a function of depth, under well controlled conditions, we employed 4 agar phantoms to simulate the acoustic and optical properties of tissue. All 4 phantoms were made of agar material, which contained a fatty emulsion to impart a "background" reduced scattering coefficient of $\mu_s' = 10cm^{-1}$. Two of the four phantoms additionally contained black ink (to impart photon absorption) as described in the following.

Phantom A1 (type A geometry**)** had no background absorption. The inner 5 mm tube contained India ink in water solution imparting an absorption coefficient of $\mu_a = 5.75cm^{-1}$ at 750 nm wavelength, which simulated the absorption of oxygenated hemoglobin in an artery. In the following this ink concentration will be referred to as the "ink solution".

Phantom A2 (type A geometry) was identical to A1, whereby the 60 mm diameter agar material further attained an average background absorption coefficient of $\mu_a = 0.25cm^{-1}$.

#166684 - $15.00 USD Received 13 Apr 2012; revised 30 Jul 2012; accepted 30 Jul 2012; published 18 Oct 2012

Phantom B1 (type B geometry) had no background absorption. The 5 mm tube contained the ink solution. The innermost tube of 1 mm diameter contained a water based solution containing ink and an optical contrast agent, AlexaFluor750 (AF750). The solution was created by adding AF750 to the ink solution until an absorption coefficient of $\mu_a = 8.05cm^{-1}$ at 750 nm was achieved.

Phantom B2 (type B) was identical to B1, but the 60 mm agar medium also attained an average absorption coefficient of $\mu_a = 0.25cm^{-1}$.

As a next step, we employed two additional phantoms made of fresh porcine muscle tissue of similar thickness as the agar phantoms, i.e. approximately 60 mm in diameter and 60 mm in height. **Phantom A3** was of type A with the 5 mm dia. tube containing the ink solution. For multi-spectral imaging a type B arrangement was also established using porcine muscle (**phantom B3**), whereby the 5 mm inner diameter and the 1 mm inner diameter tubes attained the same optical properties as in phantoms B1 and B2 (see Table 1).

Table 1. Optical Properties of Employed Phantoms at 750 nm

Phantom	60 mm cylinder		5 mm tube		1 mm tube	
	μ_s' in cm^{-1}	μ_a in cm^{-1}	μ_s' in cm^{-1}	μ_a in cm^{-1}	μ_s' in cm^{-1}	μ_a in cm^{-1}
A1	10	0	10	5.75	N/A	N/A
A2	10	0.25	10	5.75	N/A	N/A
A3	porcine tissue	porcine tissue	10	5.75	N/A	N/A
B1	10	0	10	5.75	10	8.05
B2	10	0.25	10	5.75	10	8.05
B3	porcine tissue	porcine tissue	10	5.75	10	8.05

2.3 Experimental measurements

For achieving acoustic coupling in phantom measurements, all phantoms were submerged in water using a rigid holder. Illumination was provided by an optical parametric oscillator (OPO), pumped by a Nd:YAG laser (Phocus^{TM}, Opotek Inc.). The laser produced 6 ns laser pulses with pulse energy of 50 – 90 mJ in the tunable wavelength range (690 – 900 nm) at 10 Hz repetition rate. The laser output was coupled into a fiber-bundle (Ceramoptec GmbH, Germany) with 4 branching arms, each with a 2.5 mm active inner diameter at the distal end. A rectangular region of about 40 mm length and 10 mm width was then illuminated by arranging the fiber bundles in a line, virtually 8 mm apart in front of an optical diffuser. Figure 1(c) shows the trans-illumination arrangement. For multi-spectral acquisition eleven wavelengths, equally spaced from 700 nm to 800 nm, were selected.

Ultrasonic detection was based on a custom-made 128 channel data acquisition (DAQ) system, acquiring signals in parallel with 40 Mega-samples per second. For the curved array system the digitized signals were averaged ten times; for the linear array probe 100 averages were employed to improve the signal to noise ratio due to the lower sensitivity of the linear probe, especially in the frequency range up to 3 MHz.

2.4 Image reconstruction

Image reconstruction from the acquired optoacoustic signals was performed by means of inverting a numerical forward model [18, 19]. The model is based on the forward solution of the optoacoustic wave equation given the assumption of a homogeneous speed of sound distribution within the tissue being probed. Under this assumption a measured value at the detector at time *t* can be considered the sum of all wave fronts that originated from sources with the same distance to the detector, i.e. on a sphere (or a circle if we assume a 2D slice of interest). Thus each measured value can be expressed by evaluating the forward solution of the optoacoustic wave equation on a discrete image grid. Doing this for all detector positions

#166684 - $15.00 USD Received 13 Apr 2012; revised 30 Jul 2012; accepted 30 Jul 2012; published 18 Oct 2012

and relevant time samples a system of linear equations was built, which can be separated into a model matrix, the sought after image and the acquired data. For image reconstruction we employed the Preconditioned LSQR (PLSQR) method described in [20]. Before reconstruction, the data was filtered using a bandpass with upper edge frequency of 5 MHz and a variable lower edge frequency in the range of 300 kHz. The reconstructed images were post-processed by window and leveling to improve contrast.

2.5 Multi-spectral acquisition and analysis

MSOT collects optoacoustic images at multiple wavelengths, depending on the spectral absorption profile of the chromophores of interest. Spectral analysis of this data (spectral un-mixing) can be then used to detect the spatial bio-distribution of endogenous (hemoglobin, melanin) and exogenous (contrast agents) chromophores [16]. To achieve this we applied Independent Component Analysis (ICA) [20]. The method tries to resolve the number of absorbers, their molar extinction spectra and their concentrations from the statistical properties of the whole data set. Since in a clinical setup we have some a priori information of present absorbers as well as their assumed spectra, we provided ICA with an initial guess of the spectra of AF750 and India ink, as depicted in Fig. 2(c). Subsequently ICA adapted this initial guess to better fit the data and returned the corresponding components, which represented images of the distribution of AF750 and India ink. Details of the application of the method for MSOT imaging has been analytically described in [21] and is not recapitulated herein for brevity.

2.6 In-vivo imaging of human volunteers

To confirm the observations made in phantoms and establish the feasibility of human vessel imaging, we performed imaging on human volunteers. Thereby the curved detector array was placed perpendicular on the tissue using an elastic water pad interface for optimal acoustic coupling. The water pad held the middle of the detection surface at a distance of approximately 2-3 cm from the tissue, enabling the placement of vessels at 1-3 cm tissue depth within the focus area of the detector. Illumination was provided by the same fiber illuminator placed adjacent to the curved array detector at an angle of approximately 45 degrees.

First the inner side of the lower arm around the elbow of a male volunteer was measured, because this part had been examined in previous studies [13, 21] using linear arrays. In addition, we imaged the right side of the lower neck of a female volunteer at the level of the common carotid. Both measurements were repeated at least 6 times each to establish reproducibility. To cross-validate both measurements we also acquired directional DUS images using a commercially available ultrasound system (Terason 2000 + with 12L5-V linear array, Teratech Corp.). All measurements were performed at 800 nm with the optical energy distributed in an area that was approximately 40 mm by 5 mm wide. This arrangement yielded an average light fluence of 13 mJ/cm^{-2}, which is safely below the ANSI maximum permissible skin exposure value at 800 nm (32 mJ/cm^{-2}).

3. Results

3.1 Analysis of raw signals

To study the sensitivity and the signal to noise ratio (SNR) achieved in the measurements, we performed first an analysis of raw data collected from the different phantoms. Figure 3(a) shows the signal obtained from phantom A1 captured by one of the curved array elements. The position of the absorber is clearly identified on the measurement, as indicated by the arrows.

#166684 - $15.00 USD Received 13 Apr 2012; revised 30 Jul 2012; accepted 30 Jul 2012; published 18 Oct 2012

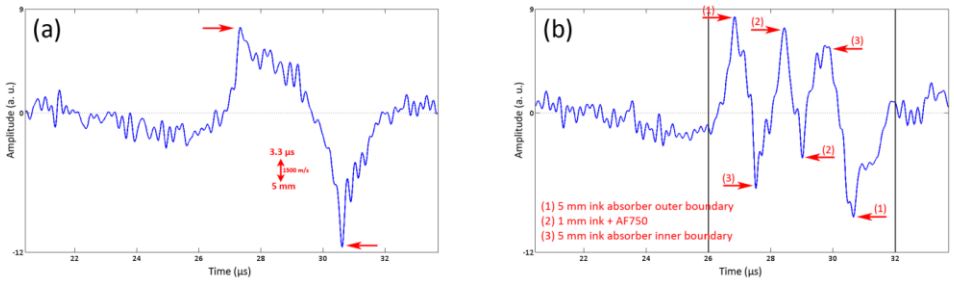

Fig. 3. Optoacoustic signal of absorber(s) within inner tube(s) from (a) phantom A1, (b) phantom B1.

Correspondingly, Fig. 3(b) shows a measurement obtained from phantom B1, detected by the same element of the curved array. Indicated by (2) is the thinner innermost absorber (1 mm), which gives a bipolar signal as in Fig. 3(a) albeit for a smaller diameter. Due to the tube-in-tube configuration a ring shaped absorber has been created by the transparent wall of the inner tube; its boundaries are indicated by (1) and (3).

To calculate the signal to noise ratio (SNR) from the raw signals collected by the curved and linear array for the type B phantoms, we analyzed data obtained from channel 32 for the curved and channel 64 for the linear array. Those channels represent a centrally located detection element placed in approximately the same position relative to the phantom imaged. Then we selected data that represented our insertion signal (absorber within the 1 mm and 5 mm tubes). In Fig. 3(b) we marked the start and end of the extracted signal data by vertical solid lines at 24 µs and 32 µs. We also selected data of equal length from the beginning of the data vectors (2-10 µs), where we expected only noise due to the extremely reduced light fluence. To obtain the SNR we calculated the root-mean-square (RMS, standard deviation) of signal and noise, and inserted them into Eq. (1):

$$SNR = 20 \log_{10}\left(\frac{Signal_{RMS}}{Noise_{RMS}}\right) \quad (1)$$

All data employed in the SNR calculation were band-pass filtered (0.1 – 5 MHz). For comparison purposes the ratio calculated for the linear array was divided by the square root of 10 before taking the logarithm to obtain the 10 average equivalent SNR. Table 2 shows the SNRs achieved by the detection geometries for phantoms of type B. Similar values can be computed for the remainder of phantoms and are thus omitted for brevity.

The results in Table 2 demonstrate the superior sensitivity of the curved geometry given the same number of averages. As expected there is also an observed drop in SNR as absorption increases in the phantom. Conversely, small SNR differences were observed between phantom B2 and the porcine muscle phantom B3; indicating that the agar phantom resembles the tissue phantom with respect to its optoacoustic properties.

Table 2. Achievable SNR

SNR	Phantom B1	Phantom B2	Phantom B3
Curved array	14.6 dB	11.1 dB	11.8 dB
Linear array	8.8[a] dB	4.1[a] dB	4.3[a] dB

[a]10 average equivalent

3.2 Curved array results

Figure 4 summarizes results obtained using the curved array detector. All image axes are given in millimeters. The images show a region of 8x8 mm centered on the phantom center.

#166684 - $15.00 USD Received 13 Apr 2012; revised 30 Jul 2012; accepted 30 Jul 2012; published 18 Oct 2012

The first column of Fig. 4 shows results from phantoms A1 and B1. The images represent the best SNR achieved in the study, because these phantoms had no background absorption; all light attenuation was only due to scattering. Figure 4(a) depicts an image of the 5 mm inner diameter tube in phantom A1 reconstructed at the 750 nm wavelength. The tube is clearly visible even at single wavelength measurements and its shape is accurately reconstructed. Stronger signal intensity appears on one side of the image due to the orientation of the illumination employed that deposited higher energy at the top part of the tube. Figure 4(d) shows in grayscale the single wavelength image (750 nm) from phantom B1 (configuration Type B, Fig. 2), whereby a 1 mm inner diameter tube was present inside the 5 mm tube. The distribution of ink in the phantom was found by spectral unmixing using ICA. The corresponding image of ink distribution is also shown on Fig. 4(d) in color. The image was thresholded to 50% of the maximum to remove background and superimposed on the single-wavelength grayscale image. In Fig. 4(d) the ink solution, present in both, 5 mm and 1 mm inner diameter, tubes, is clearly congruent with the inner volume of both tubes. The black ring shaped area, denoted as "tube wall" in Fig. 4(d), thereby represents the transparent and therefore non-absorbing wall of the 1 mm diameter tube. Figure 4(g) correspondingly shows the same single wavelength image as in Fig. 4(d), but this time the distribution of AF750, thresholded to 50% of maximum, is superimposed in color. Thus Fig. 4(g) confirms that the 1 mm tube, besides ink, also contained AF750, whereas the 5 mm tube only contained ink. For brevity, we will henceforth refer to this manner of presentation as "color overlay", i.e. a thresholded color overlay of the respective distribution (ink or AF750) on top of the same single wavelength image of the corresponding type B phantom.

The second column of Fig. 4 shows results obtained from phantoms A2 and B2. Figure 4(b) shows the reconstruction of phantom A2, whereby the 5 mm inner diameter tube is clearly visible, but with reduced contrast compared to Fig. 4(a). This is due to a weaker light intensity that reaches the 5 mm tube, due to the presence of absorption in the background medium. Figure 4(e) shows the distribution of ink as color overlay on top of a single wavelength reconstruction (in grayscale) of the 5 mm tube within phantom B2. Again, the reconstructed image confirms the presence of ink solution in both tubes (5 mm and 1 mm). Strong color variation is also observed in the background of the image in this case, because of the utilization of ink for background absorption. Figure 4(h) depicts the same single wavelength image as Fig. 4(e), with the AF750 distribution depicted as color overlay and thus confirms that spectral un-mixing accurately localized the AF750 in the 1 mm tube.

Finally the last column of Fig. 4 shows reconstruction and multi-spectral processing performance achieved from the fresh porcine muscle phantoms (A3 and B3). Figure 4(c) shows the 5 mm tube reconstructed at 750 nm from phantom A3, whereby the ink solution contained in the 5 mm tube yielded higher contrast compared to Fig. 4(b). This can be attributed to a lower than assumed absorption in the porcine tissue sample employed, due to blood drain from the muscle. In addition a stronger absorption variation is observed at the background, compared to the agar phantoms, possibly due to the higher optical heterogeneity of the tissue sample. Figure 4(f) depicts the distribution of ink in color overlaid on a single wavelength image in grayscale for phantom B3. The color overlay correctly resolves an increased absorption in both tubes (5 mm and 1 mm). Figure 4(i) depicts the distribution of AF750 superimposed in color on the grayscale image as in Fig. 4(f).

#166684 - $15.00 USD Received 13 Apr 2012; revised 30 Jul 2012; accepted 30 Jul 2012; published 18 Oct 2012

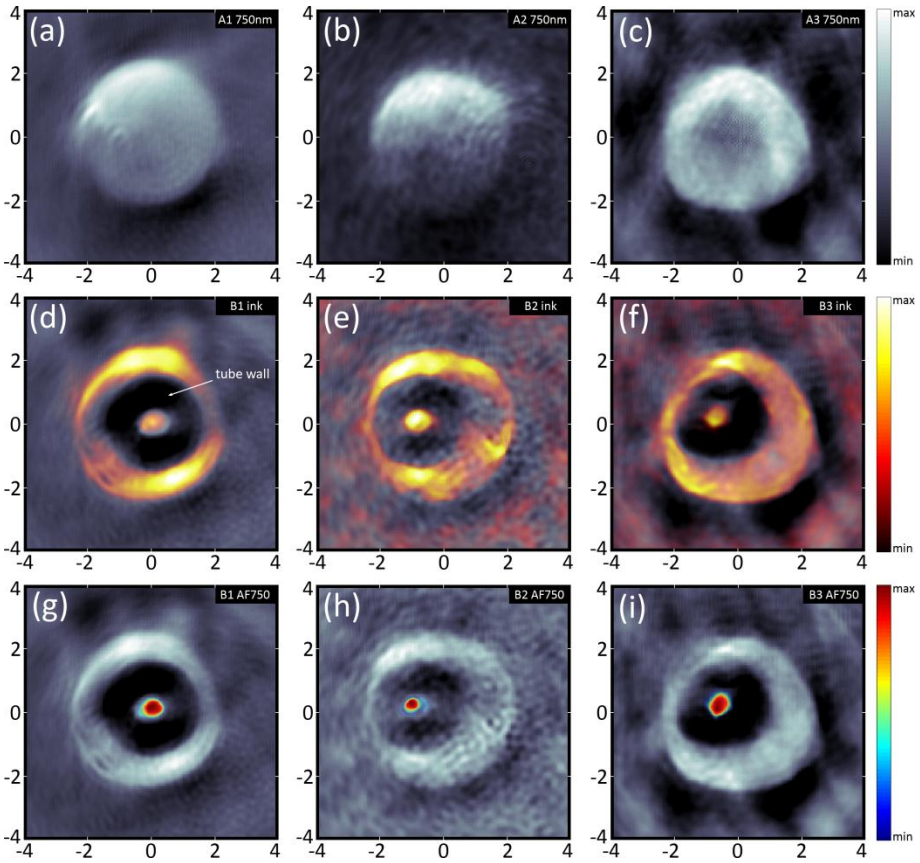

Fig. 4. Curved array reconstructions. The first row shows single wavelength images of (a) phantom A1, (b) phantom A2, (c) phantom A3. The second row shows the distribution of ink from (d) phantom B1, (e) phantom B2, (f) phantom B3. Grayscale represents a single wavelength image, whereby the color overlay shows the resolved ink concentration. The third row shows the distribution of AF750 from (g) phantom B1, (h) phantom B2, (i) phantom B3. Grayscale images are the same as in the second row; however the color overlay shows the AF750 concentration.

3.3 Linear array results

Figure 5 summarizes experimental results obtained from the linear array probe. All image axes are given in millimeters. Each image in Fig. 5 shows the same object and region with the corresponding image shown in Fig. 4.

The first column of Fig. 5 depicts results from phantoms A1 and B1. Figure 5(a) shows the reconstruction of phantom A1 at 750 nm. The ink absorber within the 5 mm diameter tube could be resolved, albeit with limited quality compared to the corresponding reconstruction using the curved array, shown in Fig. 4(a). Although changes are expected between linear and curved arrays, the image comparison between corresponding panels in Fig. 4 and Fig. 5 allows for a more detailed comparison of the relative performance achieved when using the same target but different imaging systems. Missing horizontal boundaries are a prominent feature of optoacoustic imaging with incomplete projection data (see ref [19].) and can be attributed to the highly limited angle of reception (about 68°) afforded by the linear array. Figure 5(d) shows the distribution of ink in Phantom B1, presented in color and superimposed on a single wavelength image in grayscale. Due to the severely limited quality of reconstructions in this case, we marked the boundaries of both tubes with white arrows. In Fig. 5(g) the distribution of AF750 in phantom B1 is visualized as color overlay on the same

#166684 - $15.00 USD Received 13 Apr 2012; revised 30 Jul 2012; accepted 30 Jul 2012; published 18 Oct 2012

grayscale image used in Fig. 5(d). Correspondingly ink was correctly identified in both tubes (5 mm and 1 mm), whereas AF750 was detected only within the innermost 1 mm tube.

The second column of Fig. 5 shows results for phantoms A2 and B2. As expected from the SNR analysis the single wavelength reconstruction of phantom A2, depicted in Fig. 5(b), displays more background noise, yet is qualitatively comparable to Fig. 5(a). The distribution of ink in phantom B2 is presented in Fig. 5(e) as color overlay on top a single wavelength image of phantom B2. The ink solution was correctly identified within both tubes. In addition we resolved the presence of ink within the background medium, thus confirming the result obtained from the curved array [Fig. 4(e)]. Similarly, Fig. 5(h) shows the distribution of AF750 in phantom B2. Again the AF750 content of the 1 mm tube can be localized beyond doubt.

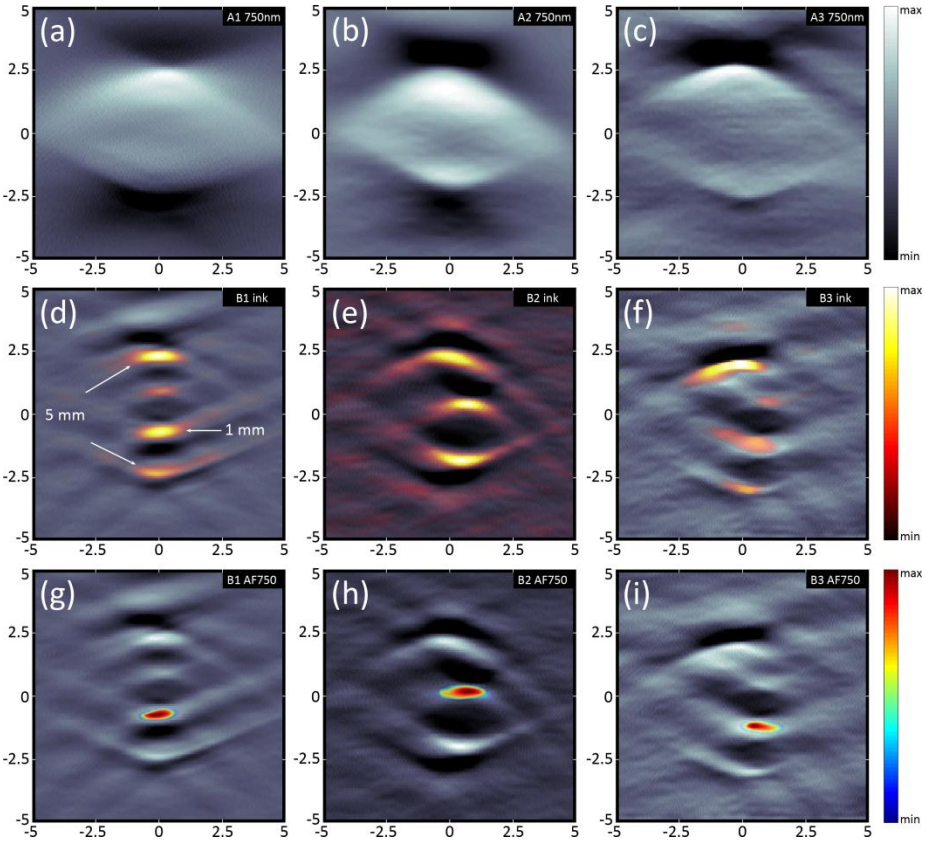

Fig. 5. Linear array reconstructions. The first row shows single wavelength images of (a) phantom A1, (b) phantom A2, (c) phantom A3. The second row shows the distribution of ink from (d) phantom B1, (e) phantom B2, (f) phantom B3. Grayscale represents a single wavelength image, whereby the color overlay shows the resolved ink concentration. The third row shows the distribution of AF750 from (g) phantom B1, (h) phantom B2, (i) phantom B3. Grayscale images are the same as in the second row; however the color overlay shows the AF750 concentration.

The third column of Fig. 5 shows results for the porcine muscle phantoms A3 and B3. Figure 5(c) represents the reconstruction of phantom A3 at 750 nm. Background noise and contrast are worse compared to Fig. 5(b), but nonetheless allow the identification of the ink solution contained in the 5 mm tube within the bounds of what is achievable with the linear array. Figure 5(f) depicts the distribution of ink in color and superimposed on a single wavelength image of phantom B2. The color overlay correctly resolves the ink solution within both tubes; however imaging and multi-spectral performance was visibly worse

#166684 - $15.00 USD Received 13 Apr 2012; revised 30 Jul 2012; accepted 30 Jul 2012; published 18 Oct 2012

compared to Fig. 5(e). Results for phantom B3 obtained from the curved array [Fig. 4(f),(i)] showed similar background artifacts. Therefore we believe that the weaker acoustic focus and limited angle of reception of the linear array affected image reconstruction for phantom B3 more than was the case for phantom B2. Nevertheless, the AF750 concentration, depicted in Fig. 5(i) in color on top of the identical grayscale image used in Fig. 5(f), could once again be identified unambiguously.

3.4 In-vivo imaging of human vasculature

We repeatedly imaged the lower arm of a male volunteer on the inner side about 7 cm from the elbow joint and obtained the same results. We therefore show in Fig. 6 a representative result thereof.

The optoacoustic image obtained at 800 nm excitation wavelength is shown in Fig. 6(a). The skin surface (marked as 1) starts at about 2 mm on the depth axis of the image and is dominated by superficial hair and small sub-cutaneous blood vessels. During imaging we applied pressure to achieve good acoustic coupling and reach deeper into the tissue. This caused a flattening of the observed veins including the intermediate antebrachial vein (marked as 2), which is seated 6-7 mm under the skin surface. Deeper into the tissue we are also able to identify the radial artery (marked as 3), which, due to the muscle of the arterial wall, shows no sign of deformation and thus allows localization at 12-14 mm from the skin surface.

For validation of the identified vasculature we show in Fig. 6(b) a directional DUS image of approximately the same measurement position. Flow directionality is represented in yellow/red for positive and green/blue for negative flow. Below the skin surface (marked as 1) we can clearly identify the intermediate antebrachial vein (marked as 2) and the radial artery (marked as 3). Both vessels appear closer to the skin surface and further apart horizontally from each other than in Fig. 6(a). This can be explained by the linear surface of the ultrasound probe, which pushed tissue and vessels horizontally apart, while the half-cylindrical surface of the optoacoustic assembly better preserved the tissue shape. The visibly lower resolution and increased shape of both vessels, but especially of the vein, are due to the choice of DUS parameters necessary to visualize the relatively weak blood flow. On the other hand the absolute position in the tissue as well as the relative position to each other corresponds very well with the optoacoustic image in Fig. 6(a).

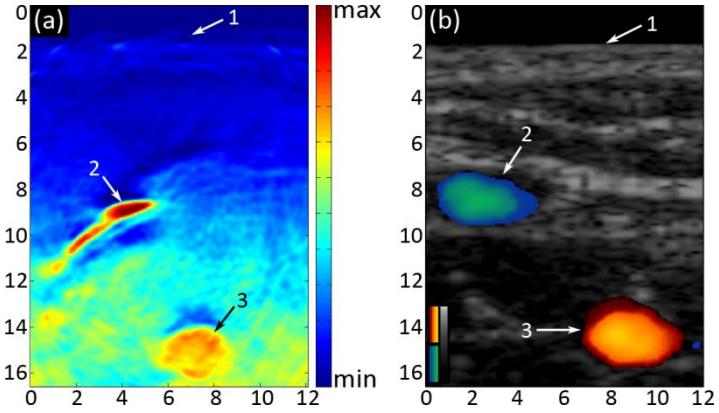

Fig. 6. Cross-sections showing lower arm vasculature of a male volunteer 7 cm from the elbow – axes are given in mm. (a) Optoacoustic image using the curved array assembly. (b) Directional DUS image indicating positive flow in yellow/red; negative flow in green/blue. Annotations: 1.Skin surface; 2.Intermediate antebrachial vein; 3.Radial artery.

As we also successfully imaged the right side of the lower neck of a female volunteer several times and obtained similar results, Fig. 7 shows a representative experimental result at the peak of the volumetric expansion caused by heartbeat.

#166684 - $15.00 USD Received 13 Apr 2012; revised 30 Jul 2012; accepted 30 Jul 2012; published 18 Oct 2012

Figure 7(a) depicts the optoacoustic image at 800 nm wavelength obtained from the curved array assembly. We can clearly identify the right common carotid (marked as 2) as it extends from 12 to 18 mm beneath the skin surface (marked as 1) and is almost perfectly round. Close by we can identify the right internal jugular vein (marked as 3), which, viewed from the skin surface, lies on top and can be divided in two separate volumes at peak expansion of the common carotid. Because of the semi-cylindrical shape of the detector as well as the applied pressure, we can also spot the external jugular vein (marked as 4). In an anatomically relaxed state of the neck we would have expected it several millimeters further to the image right.

To validate our findings we show in Fig. 7(b) a directional DUS image of approximately the same position on the lower neck. The same color maps as in Fig. 6(b) (positive flow: yellow/red; negative flow: green/blue) simplify identification of the carotid and vein. The linear array flattened the skin surface in this case (marked as 1) and also pushed the external jugular vein out of the imaging window. Because we applied less pressure than for optoacoustic imaging, the carotid (marked as 2) is shown to be seated at 13-19 mm beneath the skin surface. As expected, we also captured the internal jugular vein (marked as 3). The vascular structures observed herein correspond very well with the structures identified in the optoacoustic image.

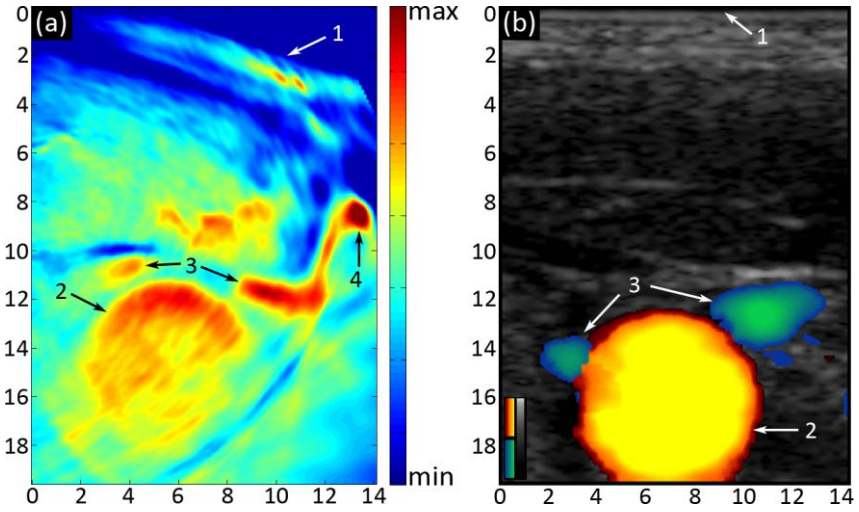

Fig. 7. Cross-sections showing cardio-vasculature of a female volunteer at the lower neck level – axes are given in mm. (a) Optoacoustic image using a curved array assembly. (b) Directional DUS image indicating positive flow in yellow/red; negative flow in green/blue. Annotations: 1.Skin surface; 2.Common carotid; 3.Internal jugular vein; 4.External jugular vein.

4. Discussion

MSOT offers complementary features to DUS for identifying functional and molecular aspects of vascular diseases. In this work we investigated the feasibility of using a clinical linear echo ultrasound detection array or a more specialized curved array for detecting deep-seated vessels such as the carotids. The phantoms employed approximated geometrical conditions associated with carotid imaging; especially close to the bifurcation level where the carotids appear 1.5-3 cm under the skin surface. The linear array employed has been a generic ultrasound sensor appropriate for a broad range of applications with respect to imaging target and depth of view. On the other hand the curved array is more appropriate for imaging a smaller volume at a fixed depth and its geometry potentially limits its broad application to various body regions. The results allow for a comparison of the relative performance achieved with linear vs. curved arrays and can offer insights into a preferred geometry for optoacoustic

#166684 - $15.00 USD Received 13 Apr 2012; revised 30 Jul 2012; accepted 30 Jul 2012; published 18 Oct 2012

carotid imaging. Furthermore the potential of the curved array was demonstrated in-vivo on human volunteers.

The results from the linear array showed that it is possible to detect absorbers of 1-5 mm sizes seated deep inside tissue. Single wavelength reconstructions provided sufficient contrast and image quality to capture insertion anatomy. In addition multi-spectral processing was deployed to locate the AF750 dye, which in a single wavelength image could not be distinguished from other absorbers. The weaknesses of the employed array, i.e. a significant number of averages and weak elevational focus, could be addressed by designing a linear probe, which is optimized with respect to sensitivity in the frequency range up to 4-5 MHz and elevational slice thickness at the depth of 15-30 mm. However a major drawback remains image quality. Missing horizontal boundaries and reduced horizontal resolution is an inherent feature of any linear array geometry in optoacoustic imaging. A probe width of about 40 mm and depth requirement of 30 mm allows us to observe our region of interest from within an angle of about 68°. In echo ultrasound this poses no problem as imaging is based on detection of reflected echoes following a directed sending pulse. In this way all interfaces, even round ones, can be imaged. Yet in optoacoustic imaging sources are generated inside the region of interest and radiate spherical waves in all directions. By limiting our view angle we therefore limit our image quality with respect to horizontal resolution.

The images derived from the curved array show markedly better imaging performance compared to the images obtained by the linear array. Shape, position and absorption values of the insertions could be resolved with much higher quality. The curved array delivers viewing angles of 172°, which offers more complete tomographic data sets that can reconstruct vessels with better fidelity. Due to the heightened sensitivity of the array around the center, compared to the linear probe, it was also possible to reduce the number of averages to manageable levels and showed potential for further reduction. Besides having its sensitivity peak at 5 MHz and thus closer to the frequency range of interest, this is due to two conceptual differences: the curved array elements are larger in size and are all looking at the same point, the center of the array. As a consequence the area around the center can be imaged with much higher sensitivity than is possible with a linear array assuming the same number of averages.

In both cases MSOT identified the absorption spectrum of a fluorochrome. The resulting images of fluorochrome distribution confirmed the performance betterment when employing the curved array, over the linear array. The ability of MSOT to image fluorescent probes is clinically appealing although the detection sensitivity needs to be investigated on a per disease and agent case. The light attenuation conditions examined herein within phantoms were an approximation of in-vivo optical properties, which were selected to be $\mu_s = 10cm^{-1}$ and $\mu_a = 0.25cm^{-1}$, modeled after average human tissue as given in Table 5.1.3 in ref [22]. Conversely, the optical properties of the porcine phantom are not an accurate representation of in-vivo condition since a significant amount of blood had been drained out from the porcine muscle imaged ex-vivo.

To establish the feasibility to detect the carotids and other deep-seated vessels in clinically relevant settings we performed imaging of human vasculature in healthy volunteers. The results showcased imaging at depths of approximately 2 cm. At these depths no signal averaging was required, which implies not only that sufficient signals were collected but also that video-rate imaging can be achieved. The frame rate of the implementation herein was determined by the pulsing frequency of the laser at 10 Hz. In this case, real-time imaging required image reconstruction within 100 ms, which is feasible in particular when employing graphic cards for fast computation. Imaging deeper in tissues was complicated not by the lack of signals from different structures but mostly by acoustic reflections from either bone or air (trachea and radius bone), which caused image artifacts. Proper optoacoustic modeling of reflective interfaces could thus allow even deeper penetration. However, reflections may not

#166684 - $15.00 USD Received 13 Apr 2012; revised 30 Jul 2012; accepted 30 Jul 2012; published 18 Oct 2012

pose a significant constraint for deeper seated carotids in cases of increased tissue thickness, especially when detectors with a larger radius are employed.

MSOT can offer significantly higher resolution over optical imaging, even when considering optical imaging methods such as early-photon tomography [23] which reduce the effects of photon scattering. Compared to single element scanning optoacoustic tomography systems [24] the use of arrays offer parallel detection performance leading to real-time imaging. Further improvements could be accomplished by the use of ultrasonic arrays arranged along two-dimensional surfaces, which are currently examined in our group as future alternatives.

Overall, this study offers the first insights that MSOT imaging of the carotids may be feasible. These results are corroborated by studies reporting that up to 7 cm of penetration depth could be achieved [15], however such estimates need to be conformed on a per case basis. The first reported in-vivo optoacoustic images of human carotids shown herein further showcase insights on the image quality that can be achieved by using curved arrays. Further imaging improvements are expected by optimizing the size and geometry of the array and the image reconstruction and spectral unmixing algorithms utilized. It has been overall hypothesized that assessment of even a small portion of the carotids may lead to obtaining risk factors of cardiovascular disease. The investigation of measuring disease relevant biomarkers using carotid MSOT will require future investigations toward better elucidating the clinical role of MSOT in cardiovascular suites.

Acknowledgments

We acknowledge funding from a MedizinTechnik award from the Bundesministerium für Bildung und Forschung (BMBF) and Prof. Ntziachristos' ERC Senior Investigator Grant (233161).

#166684 - $15.00 USD Received 13 Apr 2012; revised 30 Jul 2012; accepted 30 Jul 2012; published 18 Oct 2012